Investigating the effect of soil cracks on preferential flow using ground-penetration radar surveys and infiltration experiment in karst, Southwest China

Fang Hou[1], Jinhua Cheng[1], and Ning Guan[1]

[1]Beijing Forestry University

April 21, 2022

Abstract

Soil cracks significantly affect preferential flow; however, there are some uncertainties associated with the effect of soil cracks on preferential flow in karst areas in southwest China. In this study, ground-penetrating radar (GPR) was applied to pedons to investigate the soil crack properties (inclusion, width, and configuration). Blue dye tracing experiments were designed, based on geophysical detection results, to assess the influences of inclusions (sand grains and rock fragments), crack width (1, 1.5, and 2 cm), and configuration (I-shape, V-shape, and Λ-shape) on the preferential flow. Our results indicated that (1) GPR envelope can describe the configuration of isolated soil cracks; (2) the Brilliant Blue FCF (C.I. Food Blue 2) infiltration rate and depth were over 1.5 times slower and 1.2–3.8 times lower those of water, respectively, during infiltration; (3) soil cracks can accelerate infiltration and increase the maximum dye-penetration depth, cumulative infiltration, and wetting front depth by at least an average of 5.2% and 63.2%, respectively; and (4) the I- and Λ-shaped soil crack configurations contributed to preferential flow, while the flow was not observed along the V-shaped configuration crack pore paths. The I-shaped configurations, with a width of 1.5 cm, were filled with rock fragments and had higher preferential flow ratios (18.2%–52.3%) and length indexes (4.0%–33.8%) than those of other configurations. Inclusions, crack widths, and configurations had significant influences on preferential flow ($p < 0.05$). The influence of soil crack properties on preferential flow cannot be neglected during vegetation restoration and groundwater security processes in karst areas.

Investigating the effect of soil cracks on preferential flow using ground-penetration radar surveys and infiltration experiment in karst, Southwest China

Fang Hou[ID], Jinhua Cheng, Ning Guan

Jinyun Forest Ecosystem Station, School of Soil and Water Conservation, Beijing Forestry University, Beijing 100083, PR China

Correspondence

J. H. Cheng, Jinyun Forest Ecosystem Station, School of Soil and Water Conservation, Beijing Forestry University, Beijing 100083, PR China

E-mail: jinhua_cheng@126.com

Declaration of Interest Statement

The authors declare that they have no known competing financial interests or personal relationships that could have appeared to influence the work reported in this paper.

Abstract: Soil cracks significantly affect preferential flow; however, there are some uncertainties associated with the effect of soil cracks on preferential flow in karst areas in southwest China. In this study, ground-

penetrating radar (GPR) was applied to pedons to investigate the soil crack properties (inclusion, width, and configuration). Blue dye tracing experiments were designed, based on geophysical detection results, to assess the influences of inclusions (sand grains and rock fragments), crack width (1, 1.5, and 2 cm), and configuration (I-shape, V-shape, and Λ-shape) on the preferential flow. Our results indicated that (1) GPR envelope can describe the configuration of isolated soil cracks; (2) the Brilliant Blue FCF (C.I. Food Blue 2) infiltration rate and depth were over 1.5 times slower and 1.2–3.8 times lower those of water, respectively, during infiltration; (3) soil cracks can accelerate infiltration and increase the maximum dye-penetration depth, cumulative infiltration, and wetting front depth by at least an average of 5.2% and 63.2%, respectively; and (4) the I- and Λ-shaped soil crack configurations contributed to preferential flow, while the flow was not observed along the V-shaped configuration crack pore paths. The I-shaped configurations, with a width of 1.5 cm, were filled with rock fragments and had higher preferential flow ratios (18.2%–52.3%) and length indexes (4.0%–33.8%) than those of other configurations. Inclusions, crack widths, and configurations had significant influences on preferential flow ($p < 0.05$). The influence of soil crack properties on preferential flow cannot be neglected during vegetation restoration and groundwater security processes in karst areas.

KEYWORDS:crack, configuration, preferential flow, karst, ground-penetrating radar, Brilliant Blue FCF

1. INTRODUCTION

Karst areas in southwest China, a humid monsoon region with distinct dry and rainy seasons, are characterised by typical regional soil and vegetation that distinguish them from other regions at the same latitude (Peng et al., 2008). Carbonate-derived laterite is widely distributed in karst areas with high clay contents, low permeabilities, and high water-holding capacities (Waller and Wallender, 1993; Liu, et al., 2016; 2020). These soil features determine the calciphile and drought endurance of local vegetation (Peng et al., 2008). Moreover, the complex and unique topographical and geological conditions of karst areas lead to water and nutrient loss (Wang et al., 2019). Given these circumstances, the importance and specificity of these regions have alarmed people about their ecological conditions.

Cracks are physical phenomena that exist in clayey and expansive soils (Sima et al., 2014; Acharya et al., 2015). In karsts, the alternating wet and dry conditions and the special dilation-shrinkage characteristics of carbonate-derived laterite allow for soil cracks to form with ease (Liao et al., 2000; Zhang et al., 2021). Additionally, shallow subsurface cracks may be influenced by plant roots (Shem et al., 2009; Zhu et al., 2020), burrowing fauna (Li et al., 2019), and artificial factors (Mossadeghi-Björklund et al., 2016; Tang et al., 2016). For example, *Eucalyptus robusta* can absorb approximately 9 t hm^{-2} $year^{-1}$ of carbon dioxide while releasing oxygen (Ghannoum et al., 2010; Teixeira et al., 2020); further, rapid water absorption through its root systems result in soil crevices and cracks (Shem et al., 2009).

Cracks can enhance water infiltration and induce preferential flows (Zhang et al., 2014), making water one of the most important factors limiting karst forest development (Zhang et al., 2018; Liu et al., 2020). Preferential flow, generated by the rapid penetration of moisture through soil pore channels, is a nonuniform and unstable water flow (Bouma and De Laat, 1981; Sheng et al., 2014). Crack properties including configuration, orientation, inclusion, angle, depth, and volume can affect water distribution and preferential flow (Zhao et al., 2014). For example, the configuration of a linear crack has a high saturated hydraulic conductivity compared with other shapes and thus develops preferential flow (Liu and She, 2020), whereas regular rectangular crack networks made of steel sheets generate preferential flow only under high-intensity precipitation or irrigation conditions (Zhu et al., 2018). Inclusions within soil cracks are normally coarse particles and rock fragments in karsts (Chen et al., 2011). Although cracks and fissures in nature exist with complex combinations of properties (Zhang et al., 2014; Zhu et al., 2020), the small-scale control of the preferential flow of isolated cracks is critical for water loss in soil-epikarst zones (Liu and She, 2020).

Preferential flow visibility is usually achieved by Brilliant Blue FCF (C.I. Food Blue 2), which is a tracer that marks the area where stained water flows (Bouma and De Laat, 1981; Hagedorn and Bundt, 2002) and traces

the flow paths to reveal soil profile characteristics (Hagedorn and Bundt, 2002; Sheng et al., 2009). Recently, ground-penetrating radar (GPR) has been successfully applied to karsts to reveal structural information about the subsurface and transform invisible geological features into trended signals (Estrada-Medina et al., 2010; Fernandes et al., 2015), thereby providing more detailed information about soil profiles. GPR can accurately locate soil cracks and identify crack widths as low as 1–2 mm (Levatti et al., 2017). The combination of‘ time-lapse GPR surveys and infiltration experiments has revealed channelling soil water characteristics (Di Prima et al., 2022). However, the combination of field-based GPR data and lab-based infiltration experiments on crack properties has not been tested to generalise the flow infiltration process.

To clarify whether soil cracks enhanced preferential flow and effected infiltration processes, a case study approach was chosen. GPR was applied to physically identify the natural soil cracks and place “manmade cracks” in transparent Plexiglas columns to observe infiltration over time. This study aimed to i) identify the soil crack properties through GPR envelopes with excavated pedons; ii) evaluate the effects of crack inclusion, width, and configuration on infiltration processes and preferential flow; and iii) discuss the preferential flow characteristics caused by different cracks to further explore the infiltration mechanism in karsts.

2. MATERIALS AND METHODS

2.1 Study area

This study was conducted at 102deg54’12” E and 23deg37’13” N and an altitude of 1300–2500 m (Figure 1), in Jianshui County, Honghe Hani and Yi Autonomous Prefecture, Yunnan Province, China. This region is a karst graben basin with strong stratigraphic erosion since the Tertiary Period (Cao, 2021). The red weathering crust of carbonate rocks, known as carbonate laterite, is formed in tropical and subtropical environments through a long weathering process that is unique to the karst graben basin. The long-term average annual temperature of this area is 19.8 degC, with most of the 805 mm mean annual precipitation occurring between May and October. The summer/autumn wet season lasts from April through September and provides approximately 70%–90% of the total annual rainfall.

The *E. robusta* forests in the experimental area are approximately 1.5 km^2, which cover the Nanpan River water system in the upper reaches of the Pearl River and the middle and upper reaches of the cross-border Red River Basin. Three study sites (2.8 m x 2.8 m each) were selected for field tests and marked as Sites 1, 2, and 3. The bulk density of the soil was approximately 1.2 g/cm^3 and the pH was 6.5. Table 1 details the physical and chemical properties of the tested soil.

2.2 Experiment design

2.2.1 GRP surveys and ground truthing

This study was divided into field survey and infiltration experiment stages. The soil cracks and their properties were characterised in accordance with the GPR lines and excavation of the soil pedons using an embedded Linux GPR system (CAS-S500, IECAS, China) with a shielded antenna of 500 MHz. Horizontal and vertical GPR lines were deployed in accordance with crossed grid principles and with horizontal lines parallel to contour lines. The GPR grid (2.8 m x 2.8 m) consisted of 15 horizontal (H1–H15) and vertical (V1–V15) parallel survey lines with 20 cm between them (Figure S1). The horizontal lines were oriented downslope with a local 5deg slope. 90 radargrams (3 sites x 30 survey lines) were collected over the study area, with data acquired from the distance travelled by a survey wheel equipped with a position sensor. The sampling frequency of the system was 25.6 Hz, and the wheel moved at a uniform speed (scanning rate of 390.625 traces/s) in conformity with the survey line. The time window was set at 40 *ns* and, for each 3 m long survey transect, 258–276 traces and 38 time windows were recorded. Based on the signal fluctuations appearing in the radargrams, six pedons (three sites x two random pedons) were stochastically excavated for

verification (Figure S1). The length and depth of each pit were 120 cm and 60–70 cm, respectively. Various soil crack shapes were screened through the radargrams and pedons of the soil profile (Figure 2b).

2.2.2 Infiltration experiment design

Preferential flow paths were simulated to account for the natural cracks and pore structures of soils detected by GPR. Based on the identification of crack configuration in the field which was defined as "I", "V", and "Λ" morphologies, the infiltration experiments were conducted to explore the effect of isolated cracks on water infiltration. In addition, we found that soil cracks were filled with sand grains or rock fragments of different grain sizes when excavating the soil profile. It has been shown that inclusions (Yang et al., 2016; Liu and She, 2020), width (Ou Yang, 2020), and configuration (Liu and She, 2020) influence the infiltration process. For simplicity, soil cracks are always assumed to resemble smooth parallel plates (Tsakiroglou et al., 2012; Rouchier et al., 2012). Therefore, three properties of different inclusions (sand grains and rock fragments), crack widths (1, 1.5, and 2 cm), and configurations (I-shape, V-shape, and Λ-shape) for infiltration were simulated (Figure 2d and Table 2). A soil column without cracks (CK) was used as the control. Based on these properties, all experiments were divided into six groups (Figure 2d) in which four soil columns (including CK) were conducted simultaneously, with each experiment repeated three times.

Disturbed soil samples were collected in September 2021 from the upper 70 cm of pedons in layers. The tested soil was passed through a 2 mm sieve, air-dried, thoroughly mixed, and hierarchically backfilled into Plexiglas columns (20 cm × 5cm × 60 cm, Figure 2c) to ensure that the particle size composition of the backfilled soil was as consistent as possible with the field site. For homogeneous soil columns, the backfilled soil needed to be compacted, and the surface was roughened every 5 cm before the next layer was added. The top layer was covered with a metal mesh after backfilling soils of 50 cm to prevent water flow impact on top soils. Different crack inclusions were replaced by sand grains and rock fragments. The diameter of all sand grains was approximately 2 mm, whereas the rock fragments ranged 2–5 mm. All these debris (i.e. sand grains and rock fragments) was wrapped with 500-mesh nylon netting to prevent soil particles from passing through and blocking the paths (Figure 2c). From the field excavation of representative sites and GPR large-scale detection, cracks are mainly scattered approximately 10 cm from the surface. Therefore, the lab-based experiments of cylindrical "channel" was placed in column when backfilled to 30 cm from the upper edge of the column to simulate various cracks.

Brilliant Blue FCF allows clear visualisation of the infiltration process of non-uniform flow in the soil (Lipsius et al., 2006); as such, a Brilliant Blue FCF dye volume of 5 L (4 g/L) was added to the Marriott bottles to visualise the preferential flow paths. The volume of the dye solution used corresponded to the amount of water collected in a 20 mm rainfall event, considering more than 65% of regional rainfall events were for 20 mm during 2009–2018. Therefore, a constant pressure head of 20 mm was supplied using Marriott bottles (Figure 2c). For each experimental group, four images (three variances and a control) were taken with a digital camera (Canon EOS 60D, Canon, Japan) directly in front of the soil column at 3, 5, 10, 20, 30, 50, 70, and 90 minutes after the Brilliant Blue FCF dye solution was applied. The infiltration continued until the wetting front penetrated the bottom of the column. The dye infiltration depth and wetting front trajectory of each soil column were recorded simultaneously using a ruler with millimetre precision attached to the edge of the soil column. The infiltration rate was determined by measuring change in water level in Marriott bottles over time.

2.3 Data analysis

2.3.1 GPR data processing

GPR data were processed following a conventional routine (Dal et al., 2019; Guo et al., 2014) via Radar View V18.08 (Institute of Electronics, Chinese Academy of Science, China) to enhance the signal-to-noise ratio, which follows the sequence: 1) background filter wiped off antenna reverberation; 2) time-zero correction calibrated the radar antenna start time; 3) energy gained compensated energy attenuation with propagation

depth; 4) Hilbert filter removed high- and low-frequency; and 5) DC-drift suppressed low-frequency noise and remedied average amplitude. Finally, the high signal areas float compared to their surroundings in the radargram, and were converted to average envelope curves (Figure 2a). The envelopes can estimate the configuration of soil cracks, and the abnormal signals, defined as cracks on the radargram, were used to calculate the soil crack densities at the study site. Total amplitude area (TotAra) is the area enclosed by the envelope curve and the coordinate axis. Accumulative amplitude ($\mathrm{Acum_a}$) is the accumulation of the amplitude at every 1 cm soil depth on the envelope curve (The crack signal illustration method is shown in Figure S2).

2.3.2 Image processing and data analysis of preferential flow

The captured images were cropped, and the threshold was adjusted using Photoshop 2020 (Adobe Systems Inc., San Jose, CA) for further analysis. The stained area was replaced with black (0) and the non-stained area was replaced with white (255) via the colour replacement function. Separation was then conducted using Image Pro Plus 6.0 (Media Cybernetics Inc., Rockville, MD) to obtain only 0 and 255 dual-value matrices after bitmap analyses were done.

Dye coverage (D_C) is defined as the ratio of the stained area to the total soil vertical profile, and the area was measured using a matrix converted from pixel grids and was calculated as follows:

, (1)

where D is the number of matrix values of 0 andN_D is the number of matrix values of 255.

Many historians have argued that the matrix flow depth (U_F) is defined as the depth at which the stained area ratio is greater than 80% (Schaik, 2009; Bargues Tobella et al., 2014). In contrast to preferential flow, water infiltration in the matrix flow region is relatively uniform and continuous. Matrix flow often leads to a delay in the preferential flow.

The preferential flow ratio (P_F) is defined as the ratio of the stained area of the preferential flow area to the entire vertical profile; a high P_F value leads to a high degree of preferential flow. This can be calculated as follows:

, (2)

where W is the width of the Plexiglas column (W = 20 cm) and D_T is the total stained area of the soil profile (cm^2).

The length index of preferential flow (L_i) describes the heterogeneity of the dye penetration, which is higher in the preferential flow region than in the matrix flow region. A high L_i value leads to a high degree of preferential flow. This can be calculated as follows:

, (3)

where n is the number of vertical soil layers in the soil profile (one pixel down along the vertical profile named one layer, the size of which is determined by the number of pixels contained in the maximum infiltration depth), and $D_{c(i+1)}$ andD_{ci} are the stained area ratios corresponding to soil profile layer i +1 and i , respectively.

3. RESULTS

3.1 Soil profile characteristics

The general characteristics of soil pedons are illustrated based on pedon 1 (Figure 2b). At 0–10 cm soil depth, the soil was dark red with numerous wormholes found due to the high organic matter content of the surface layer. Cracks began to appear below 10 cm, with a few soil profiles showing various crack configurations. For

instance, pedon 1 contained a V-shaped crack at 18–21 cm and an I-shaped crack at approximately 19–33 cm, while most of the profiles contained more I-shaped cracks. Pedon 1 consisted of four genetic horizons, delineated as A (0–8 cm), B1 (8–21 cm), B2 (21–54 cm), and BC (54–60 cm) (Figure 2b), which were classified as loamy skeletal, mixed, super-active, or mesic, respectively (Soil Survey Staff, 1999).

This experiment applied GPR technology to physically probe soil cracks and identify natural crack configurations before the infiltration experiment was unfolded. High-signal areas floating on the radargrams were identified, and the envelopes were calculated as the average crack coverage amplitude (Table 3). Soil cracks existed or did not result in different envelopes. The envelope of non-crack profiles had no substantial fluctuation with reflection wave conduction, while the profile with cracks showed more signal fluctuations at 0.3–0.6 m. The extracted crack signal parameters $\mathrm{TotAr_a}$, $\mathrm{Max_a}$, $\mathrm{Min_a}$, and $\mathrm{Acum_a}$support the phenomenon (Table 3). Furthermore, the amplitude fluctuation of the I-shaped crack was less marked than that of the V- and Λ-shaped cracks (Figure S3). Thus, the different soil crack configurations, as determined by GPR and excavation, could provide practical support for conducting infiltration experiments. Notably, geophysical methods cannot directly explain all the properties of soil cracks. Whether the crack width, inclusion, and signal fluctuations corresponded to each other based on the raw data remains unclear.

3.2 Comparison between Brilliant Blue FCF solution and water transport

Figure 3 shows the infiltration trajectories with time, showing that the Brilliant Blue FCF solution penetrates faster than water. The difference between water and dye penetration was observed at the beginning of infiltration, as early as 3 min. In the VR1.5 treatment (Figure 3c), the matrix flow was notably dominant throughout the infiltration process, and no preferential flow occurred. This phenomenon indicates that water was probably not transported down V-shaped cracks (Figure 3b). The matrix flow dominated before 30 min, while preferential flow dominated later in the IR1.5 and ΛR1.5 treatments (Figure 3a–b).

The dye-stained and wetting areas show a linear fit with the primary function, in which the R^2 values were all above 0.8 (Figure 4). Regarding the I-shaped crack filled with rock fragments, slight variabilities were found between Brilliant Blue FCF solution and water when the dye-stained area was less than 21%, at which point the former infiltrated marginally faster than the latter; however, these differences gradually became more potent after the turning point, indicating that there was a lag in the effects of the Brilliant Blue FCF solution compared to water (Figure 3–4). Comparison with the I-shaped crack showed that the retardation on the solution infiltration in the Λ-shaped crack appeared later, around a dye-stained area ratio of 24%–27%. This result may explain, at least in part, that the retardation on the Brilliant Blue FCF with time was influenced by the crack configuration, and the flow pathways of the Brilliant Blue FCF were not fully representative of water infiltration paths.

3.3 Effect of crack properties on infiltration and preferential flow

The effects of the crack properties (inclusion, crack width, and configuration) on the infiltration rate, maximum dye-penetration depth, cumulative infiltration, and wetting advancing rate are shown in Figure 5–7. Generally, a noticeable trend in the infiltration rate was observed, which could be divided into a sharp decline and a steady decline for all treatments. The turning point occurred at approximately 40 min, after which, the infiltration rate reached a relatively smooth decline for all treatments (Figure 5a, 6a, and 7a). The maximum dye penetration depth and cumulative infiltration increased at a slower rate with time after 40 min (Figure 5b–c, 6b–c, and 7b–c).

3.3.1 Crack inclusion

Regarding the influence of inclusions, the infiltration rate was faster by 18.8% on average when filled with rock fragments than when filled with sand grains (Figure 5a), and the existence of cracks increased the dye-penetration depth, cumulative infiltration, and wetting front depth by at least 5.2%, 63.2%, and 4.4% (Figure 5b–d). These results were apparent in the IR2, IS2, ΛR1.5, and ΛS1.5 treatments, indicating that cracks

filled with rock fragments enhanced the infiltration capacity of the soil. The ΛR1.5 treatment had a notably higher dye penetration depth, cumulative infiltration, and wetting front depth at the end of infiltration (Figure 5b–d). For example, the 70-min wetting front depth of the ΛR1.5 treatment was 46.5 mm, whereas that of the ΛS1.5 treatment decreased by 17.0 % (Figure 5d). Similarly, the maximum dye-penetration depth and cumulative infiltration decreased by 14.9% and 4.4%, respectively (Figure 5b–c).

3.3.2 Crack width

The volumes corresponding to the three crack widths were 8.0, 17.5, and 31.5 cm^3, respectively. Regarding crack widths, significant differences (p <0.05) were identified in the infiltration rates among the three treatments with different crack widths (Figure 8b). After the infiltration reached relative stability, the infiltration rate was faster for the 1.5-cm width crack (Figure 6a). The maximum dye-penetration depth, cumulative infiltration, and wetting advancing rate were the highest when the crack width was 1.5 cm (Figure 6b–d), and there was a significant difference (p <0.05) in the maximum dye-penetration depth with the 1.5-cm width crack (Figure 8b). Our experimental results indicate the existence of a certain optimal crack width between 1 and 2 cm, which allowed the infiltration rate to be maximised. After the crack volume reached a value range of 8.0–31.5 cm^3, moisture was more inclined to be stored in the crack than to infiltrate downward.

3.3.3 Crack configuration

Regarding the configuration, the chart shows that the ΛR1.5 treatment had a substantially higher penetration rate than other configurations, ranging from 54% to 120% higher than other two configurations (Figure 7a). The maximum dye-penetration depth and cumulative infiltration of the Λ-shaped configuration increased steadily at the beginning of infiltration, crossing the line for the I-shaped configuration at approximately 50 min (Figure 7b and 7c). When infiltration proceeded to a certain process, the Λ-shaped configuration increased the rate of liquid passage, but the effect on the wetting advancing rate was not obvious. The wetting front depth nearly overlapped between the three crack configurations, with variations ranging from 0.03% to 38.39% (Figure 7d). Significant differences (p <0.05) were observed between the IR1.5 and ΛR1.5 treatments, but there were no significant differences (p <0.05) between these and the VR1.5 treatment (Figure 8c).

3. 4 Contribution of crack properties to preferential flow

The I- and Λ-shaped treatments, filled with rock fragments, generated preferential flow, whereas the V-shape was not sensitive to preferential flow (Table 2). Thus, the analysis of dye coverage and preferential flow indices was displayed only for IR1, IR1.5, IR2, and ΛR1, ΛR1.5, and ΛR2 treatments.

Figure 9 illustrates the turning range of the preferential flow ratio with increasing crack width for the same configuration and inclusion. The experiment proved that the preferential flow extensively slowed down the decline in dye coverage and remained steady in the IR1.5 and ΛR2 treatments (Figure 9b and 9f). For example, the percentage of preferential flow dye coverage in the IR1.5 treatment ranged from 60.7% at 15 cm to 14.4% at 20 cm, while in the ΛR1.5 treatment, it ranged from 75.9% at 14 cm to 7.5% at 17 cm. The variations indicated more preferential pathways in the ΛR1.5. However, a rebound point at a soil depth of 15 cm was observed in the IR2 treatment, in which the morphology of the stained end appeared radially orbicular (Figure 9c). This demonstrates the configuration has a greater effect on preferential flow and a wider linear crack filled with rock fragments likely leads to a lateral flow at the end of the crack.

Overall, the preferential flow ratio increased with increasing crack width, similar to the length index of the preferential flow. Generally, the preferential flow ratio and matrix flow depth showed opposite trends; however, this was not always the case (Table 4). Treatment with IR1.5, however, did not match the above regularity. The nonuniformity and spatial variability of the linear crack was more distinct, which led to an obvious preferential flow phenomenon. The response of the Λ-shaped crack to the preferential flow with time

lagged. For instance, the depth of matrix flow for I-shape was 0.9%–33.3% lower than that for Λ-shape; however, the length index of preferential flow was higher by 3.9%–11.4% (Table 4).

4. DISCUSSION

4.1 Effect of crack properties on preferential flow

During the infiltration event, the infiltration rate of Brilliant Blue FCF was over 1.5 times slower and the infiltration depth was 1.2–3.8 times lower than those of water, which may be attributed to the fact that the viscosity of water was different from that of Brilliant Blue FCF. A similar phenomenon was observed by Liu and She (2020a), who showed that a large organic molecule size and nonlinear adsorption behaviour within the soil matrix led to slow migration rates. This may be due to the retardation caused by the reaction between Brilliant Blue FCF and Ca^{2+} in carbonate laterite areas (Flury and Flühler 1995; Nobles et al., 2010). Therefore, using Brilliant Blue FCF as a staining tracer, the infiltration depth in the soil profile may not be the true water infiltration depth. The results of this experiment can be used as a basis for calibration in future field tests.

Soil cracks showed undulated reflections and individual features, whereas CK showed a more continuous interface, as derived from the envelope curves (Figure S3). Moreover, the morphological characteristics in the vertical direction of the I-shaped cracks showed a smaller envelope reflection amplitude than those of the other shapes. Cracks are always filled with sand grains or rock fragments, which had a significant role in providing high-amplitude reflections (Han et al., 2016; Dal et al., 2019*)* . Although the co-offset results only distinguished the envelope curves of different crack configurations, the soil cracks always had different widths and inclusions as well (Tsakiroglou et al., 2012; Yang et al., 2016), where the radar reflections provided by could not be distinguished.

The volume proportion of "manmade cracks" occupied approximately 0.16%, 0.35%, and 0.63%, corresponding to the 1-, 1.5-, and 2-cm cracks, respectively, as shown in the infiltration experiments. Although the volume of cracks was less than 1%, the existence of cracks considerably accelerated the water infiltration rate, while the infiltration rate, maximum dye-penetration depth, cumulative infiltration, and wetting advancing rate of CK were lower than those of other treatments containing cracks. Cracks provide channels or pores for fluid flow, even though only the I- and Λ-shaped cracks produce preferential flow. Our findings did not concur with those of Liu and She (2020a), who suggested that crack volume is not a good predictive parameter for infiltration characteristics. However, Yang (2020) concluded that the crack volume is an important indicator of the initial infiltration rate, and that they are positively correlated.

Preferential flow was observed only in the I- and Λ-shaped treatments, along the crack pore paths. These results are consistent with those of Liu and She (2020a) and Yang et al. (2016), who demonstrated that cracks influence preferential flow. Liu and She (2020a) showed that I-shaped cracks retained more water than V-shaped or non-cracks, in which preferential flow was the dominant flow type. Yang et al. (2016) revealed that the orientation of subsurface flow varied in accordance with the connectivity of the cracks or underlying structure, which resulted in lateral flows and deep percolation occupying approximately 32%–36% of the total rainfall.

4.2 Necessity of combining geophysical surveys and column experiments

GPR was successfully applied in karst topography to reveal structural information about the subsurface and achieve the transformation of invisible geological features into trended signals (Estrada-Medina et al., 2010; Fernandes et al., 2015), thus providing more detailed information about soil profiles (Busch et al., 2013). This geophysical technique retrieves information with the advantages of low-cost, efficiency, and less labour-intensive. We explored the distribution and characteristics of soil cracks on a large scale in the field, and verified the configuration by GPR. On the one hand, geophysical surveys provide a reference for the crack

properties before the simulation experiments. The column experiments were conducted based on the results of GPR and excavations and visualise the flow infiltration process (Liu et al., 2020a). On the other hand, it provides a new insight for interpreting isolated cracks from radar signals. The combination of GPR with field observations and column experiments has shown great potential for investigate the effect of isolated soil cracks on preferential flow.

5. CONCLUSIONS

In this study, field GPR physical imaging techniques and infiltration experiments were applied to investigate the effects of crack properties on preferential flow paths. Many soil cracks filled with fine fragments were present in karst. By evaluating the influence of crack inclusion (sand grains and rock fragments), crack width (1, 1.5, and 2 cm), and configuration (I-shape, V-shape, and Λ-shape) on infiltration, we found that isolated soil cracks could enhance preferential flow with some properties.

The isolated soil cracks accelerated the infiltration process supported by infiltration rate, maximum dye-penetration depth, cumulative infiltration, and wetting advancing rate. These indicators reached a relatively stable increase or decrease in infiltration over time until the 40th min. The transport depth of Brilliant Blue FCF was 1.2–3.8 times slower and the infiltration rate was over 1.5 times slower than that of water during the entire infiltration process. The retardation of the Brilliant Blue FCF necessitates calibration when applied to field infiltration tests.

The inclusions, crack width, and configuration significantly affected the preferential flow indices ($p < 0.05$), of which the configuration has a greater effect on preferential flow. Only I-shape and Λ-shape of the soil cracks filled with rock fragments generated preferential flow. The effect of linear cracks on preferential flow in the field cannot be ignored.

The configuration of isolated soil cracks can be identified by GPR envelopes. The GPR envelope can be used to directly reflect the possible occurrence of preferential flow during rainfall conditions in crack soils.

Our research proved that isolated cracks control preferential flow and relationships between envelopes and preferential flow indices in crack soils. These findings offer new insights for underground hydrological processes and vegetation restoration in karst areas. Further research should be directed towards the future development of a combination of complex crack structures at large scales.

ACKNOWLEDGMENTS

This research was financially supported by The National Natural Science Foundation of China (32071839). The authors thank Ning Guan and Zhiming Niu for helping with the field work, and American Journal Experts for English language editing.

CONFLICT OF INTEREST STATEMENT

The authors declare that they have no known competing financial interests or personal relationships that could have appeared to influence the work reported in this paper.

DATA AVAILABILITY STATEMENT

The data that support the findings of this study are available from the corresponding author upon reasonable request.

References

Acharya, R., Pedarla, A., Bheemasetti, T. V., Puppala, A. J., Zhang, N., 2015. Shrinkage induced pressure measurement to address desiccation cracking in expansive soils. Geotech. Special Publication, pp. 2122-2130. https://doi.org/10.1061/9780784479087.196

Bargues Tobella, A., Reese, H., Almaw, A., Bayala, J., Malmer, A., Laudon, H., Ilstedt, U., 2014. The effect of trees on preferential flow and soil infiltrability in an agroforestry parkland in semiarid Burkina Faso. Water Resources Research 50 (4), 3342-3355. https://doi.org/10.1002/2013wr015197

Bouma, J., De Laat, P. J. M., 1981. Estimation of the moisture supply capacity of some swelling clay soils in the Netherlands. Journal of Hydrology 49, 247-259. https://doi.org/10.1016/0022-1694(81)90216-x

Busch, S., Weihermüller, L., Huisman, J. A., Steelman, C. M., Endres, A. L., Vereecken, H., van der Kruk, J., 2013. Coupled hydrogeophysical inversion of time-lapse surface GPR data to estimate hydraulic properties of a layered subsurface. Water Resour. Res. 49, 8480–8494. https://doi.org/10.1002/2013wr013992

Cao, J. H., 2021. Guest Editor's Preface to the "Critical Zone and Eco Geological Environment in the Karst Graben Basin". Acta Geoscientica Sinica, 42 (3), 4. https://doi.org/10.3975/cagsb.2021.032901

Chen, H., Liu, J., Wang, K., Wei, Z., 2011. Spatial distribution of rock fragments on steep hillslopes in karst region of northwest Guangxi. China. CATENA 84, 21–28. https://doi.org/10.1016/j.catena.2010.08.012

Dal Bo, I., Klotzsche, A., Schaller, M., Ehlers, T. A., Kaufmann, M. S., Fuentes Espoz, J. P., Vereecken, H., van der Kruk, J., 2019. Geophysical imaging of regolith in landscapes along a climate and vegetation gradient in the Chilean coastal cordillera. CATENA 180, 146-159. https://doi.org/10.1016/j.catena.2019.04.023

Di Prima, S., Giannini, V., Ribeiro Roder, L., Giadrossich, F., Lassabatere, L., Stewart, R. D., Abou Najm, M. R., Longo, V., Campus, S., Winiarski, T., Angulo-Jaramillo, R., del Campo, A., Capello, G., Biddoccu, M., Roggero, P. P., Pirastru, M., 2022. Coupling time-lapse ground penetrating radar surveys and infiltration experiments to characterize two types of non-uniform flow. Science of The Total Environment 806, 150410. https://doi.org/10.1016/j.scitotenv.2021.150410

Estrada-Medina, H., Tuttle, W., Graham, R. C., Allen, M. F., Jiménez-Osornio, J. J., 2010. Identification of underground karst features using ground penetrating radar in northern Yucatán, México. Vadose Zone 9, 653-661. https://doi.org/10.2136/vzj2009.0116

Fernandes, A. L., Medeiros, W. E., Bezerra, F. H. R., Oliveira, J. G., Cazarin, C. L., 2015. GPR investigation of karst guided by comparison with outcrop and unmanned aerial vehicle imagery. Appl. Geophys 112, 268-278. https://doi.org/10.1016/j.jappgeo.2014.11.017

Flury, M., Flühler, H., 1995. Tracer characteristics of Brilliant Blue FCF. Soil Sci. Soc. Am. J. 59, 22-27. https://doi.org/10.2136/sssaj1995.03615995005900010003x

Ghannoum, O., Phillips, N. G., Conroy, J. P., Smith, R. A., Attard, R. D., Woodfield, R., Logan, B. A., Lewis, J. D., Tissue, D. T., 2010. Exposure to preindustrial, current and future atmospheric CO_2 and temperature differentially affects growth and photosynthesis in Eucalyptus. Global Change Biology 16 (1), 303-319. https://doi.org/10.1111/j.1365-2486.2009.02003.x

Guo, L., J. Chen, and H. Lin (2014), Subsurface lateral preferential flow network revealed by time-lapse ground-penetrating radar in a hillslope, Water Resour. Res., 50. https://doi.org/10.1002/2013wr014603

Hagedorn, F., Bundt, M., 2002. The age of preferential flow paths. Geoderma 108, 119-132. https://doi.org/10.1016/s0016-7061(02)00129-5

Han, X. L., Liu, J. T., Zhang, J., Zhang, Z. C., 2016. Identifying soil structure along headwater hillslopes using ground penetrating radar based technique. Journal of Mountain Science 13 (3), 405-415. https://doi.org/10.1007/s11629-014-3279-7

Levatti, H. U., Prat, P. C., Ledesma, A., Cuadrado, A., Cordero, J. A., 2017. Experimental analysis of 3D cracking in drying soils using ground-penetrating radar. Geotechnical testing journal, 40 (2), 221-243. https://doi.org/10.1520/gtj20160066

Li, T. C., Shao, M. A., Jia, Y. H., Jia, X. X., Huang, L. M., Gan, M., 2019. Small-scale observation on the effects of burrowing activities of ants on soil hydraulic processes. Eur. J. Soil Sci. 70, 236-244. https://doi.org/10.1111/ejss.12748

Liao, Y. L., Zhang, Z. R., Zhou, X., 2000. Understanding of the dilation shrinkage characteristic of guizhou carbonate derived laterite based on karstification. Carsologica Sinica, 19 (4), 342-346. https://doi.org/10.3969/j.issn.1001-4810.2000.04.008

Lipsius, K., Mooney, S. J., 2006. Using image analysis of tracer staining to examine the infiltration patterns in a water repellent contaminated sandy soil. Geoderma 136, 865-875. https://doi.org/10.1016/j.geoderma.2006.06.005

Liu, D. D., She, D. L., 2020b. Combined effects of moss crusts and pine needles on evaporation of carbonate-derived laterite from karst mountainous lands. Journal of Hydrology, 586, 124859. https://doi.org/10.1016/j.jhydrol.2020.124859

Liu, D. D., She, D. L., 2020a. The effect of fracture properties on preferential flow in carbonate-derived laterite from karst mountainous agroforestry lands. Soil and Tillage Research 203. https://doi.org/10.1016/j.still.2020.104670

Liu, M. X., Xu, X. L., Wang, D. B., Sun, A. Y., Wang, K. L., 2016. Karst catchments exhibited higher degradation stress from climate change than the non-karst catchments in southwest China: An ecohydrological perspective. J. Hydrol. 535, 173-180. https://doi.org/10.1016/j.jhydrol.2016.01.033

Mossadeghi-Björklund, M., Arvidsson, J., Keller, T., Koestel, J., Lamandé, M., Larsbo, M., Jarvis, N., 2016. Effects of subsoil compaction on hydraulic properties and preferential flow in a Swedish clay soil. Soil Tillage Res. 156, 91-98.

Nobles, M. M., Wilding, L. P., Lin, H. S., 2010. Flow pathways of bromide and Brilliant Blue FCF tracers in caliche soils. J. Hydrol. (Amst) 393, 114-122. https://doi.org/10.1016/j.still.2015.09.013

Ou Yang, G. Q., 2020. Research on Effect of Grain-size Composition and Cracking State on Collapsing Gully Erosion. MA thesis, Nanchang University, Nanchang, China.

Peng, W. X., Wang, K. L., Song, T. X., Zeng, F. P., Wang, J. R., 2008. Controlling and restoration models of complex degradation of vulnerable karst ecosystem. Acta Ecologica Sinica 28 (2), 811-820. https://doi.org/10.3321/j.issn:1000-0933.2008.02.044

Rouchier, S., Janssen, H., Rode, C., Woloszyn, M., Foray, G., Roux, J. J., 2012. Characterization of fracture patterns and hygric properties for moisture flow modelling in cracked concrete. Construction and Building Materials 34 (3), 54-62

Schaik, N., 2009. Spatial variability of infiltration patterns related to site characteristics in a semi-arid watershed. CATENA 78 (1), 36-47. https://doi.org/10.1016/j.conbuildmat.2012.02.047

Shem, K., Catherine, M., Ong, C., 2009. Gas exchange responses of*Eucalyptus, C. africana* and *G. robusta* to varying soil moisture content in semi-arid (Thika) Kenya. Agroforestry Systems 75 (3), 239-249. https://doi.org/10.1007/s10457-008-9176-8

Sheng, F., Kang, W., Zhang, R. D., Li, E., 2009. Study on heterogeneous characteristics of soil water flow in field by dye tracing method. Shui Li Xue Bao 40 (1), 101-108. https://doi.org/10.3321/j.issn:0559-9350.2009.01.015

Sheng, F., Liu, H., Kang, W., Zhang, R., Tang, Z., 2014. Investigation into preferential flow in natural unsaturated soils with field multiple-tracer infiltration experiments and the active region model. Journal of

Hydrology 508 (3) 137-146. https://doi.org/10.1016/j.jhydrol.2013.10.048

Sima, J., Jiang, M., Zhou, C., 2014. Numerical simulation of desiccation cracking in a thin clay layer using 3d discrete element modeling. Computer and Geotechnics, 56 (3), 168-180. https://doi.org/10.1016/j.compgeo.2013.12.003

Soil Survey Staff, 1999. Soil taxonomy: A basic system of soil classification for making and interpreting soil surveys. US Department of Agriculture, National Resources and interpreting soil surveys. US Department of Agriculture, National Resources Conservation Service, Washington, DC.

Tang, Y., Sun, K., Zhang, X., Zhou, J., Yang, Q., Liu, Q., 2016. Microstructure changes of red clay during its loss and leakage in the karst rocky desertification area. Environ. Earth Sci. 75, 537. https://doi.org/10.1007/s12665-016-5419-6

Teixeira, R. D. S., Fialho, R. C., Costa, D. C., Nogueira de Sousa, R., Santos, R. S., Teixeira, A. P. M., Reis, T. G., Ribeiro da Silva, I., 2020. Land-use change with pasture and short rotation eucalypts impacts the soil C emissions and organic C stocks in the Cerrado biome. Land Degradation & Development 31 (7), 909-923. https://doi.org/10.1002/ldr.3480

Tsakiroglou, C. D., Klint, K. E. S., Nilsson, B., Theodoropoulou, M. A., Aggelopoulos, C. A., 2012. From aperture characterization to hydraulic properties of fractures. Geoderma 181-182, 65-77. https://doi.org/10.1016/j.geoderma.2012.02.027

Waller, P. W., Wallender, W. W., 1993. Changes in cracking, water content and bulk density of salinized swelling clay field soils. Soil Science 156, 414-423. https://doi.org/10.1097/00010694-199312000-00006

Wang, K, Zhang, C., Chen, H., Yue, Y., Fu, Z., 2019. Karst landscapes of China: Patterns, ecosystem processes and services. Landscape Ecology 34 (3), 2743-2763. https://doi.org/10.1007/s10980-019-00912-w

Yang, J., Nie, Y., Chen, H., Wang, S., Wang, K., 2016. Hydraulic properties of karst fractures filled with soils and regolith materials: implication for their ecohydrological functions. Geoderma 276, 93-101. https://doi.org/10.1016/j.geoderma.2016.04.024

Zhang, J. M., Luo, Y., Zhou, Z., Chong, L., Victor, C., Zhang, Y. F., 2021. Effects of preferential flow induced by desiccation cracks on the slope stability. Engineering Geology, 288, 106164. https://doi.org/10.1016/j.enggeo.2021.106164

Zhang, R., Xu, X., Liu, M., Zhang, Y., Xu, C., Yi, R., Luo, W., 2018. Comparing evapotranspiration characteristics and environmental controls for three agroforestry ecosystems in a subtropical humid karst area. J. Hydrol. (Amst) 563, 1042-1050. https://doi.org/10.1016/j.jhydrol.2018.06.051

Zhang, Z. B., Zhou, H., Zhao, Q. G., Lin, H., Peng, X., 2014. Characteristics of cracks in two paddy soils and their impacts on preferential flow. Geoderma 228-229, 114-121. https://doi.org/10.1016/j.geoderma.2013.07.026

Zhao, S. L., 2014. The characteristics of fissures development in deposits and its effects on rainfall infiltration process—Taking the Meilishi 3# Landslide as an example. MA thesis, Chengdu University of Technology, Chengdu, China.

Zhu, L., Fan, D., Ma, R., Zhang, Y., Zha, Y., 2018. Experimental and numerical investigations of influence on overland flow and water infiltration by fracture networks in soil. Geofluids 2018, 1-16. https://doi.org/10.1155/2018/7056858

Zhu, L., Shen, T., Ma, R., Fan, D., Zha, Y., 2020. Development of cracks in soil: an improved physical model. Geoderma, 1 (1), 1. https://doi.org/10.1016/j.geoderma.2020.114258

Figures caption:

FIGURE 1 Location of research area and the three study sites in Jianshui County, Yunnan Province, China.

FIGURE 2 Main steps of infiltration experiment: (a) identification of envelope curves on radargram; (b) soil profile at pedon 1 (yellow dotted lines represent the boundary between horizons, white dashed boxes represent cracks found during excavation); (c) Plexiglas columns for experiment and text device; and (d) experimental groups to be performed.

FIGURE 3 Infiltration process over time in different treatments (only IR1.5, ΛR1.5, and VR1.5 treatments are shown here), with blue lines indicating dye traces, yellow lines indicating moisture wetting front traces, and red dotted regions indicating that the preferential flow occurred after 40 minutes.

FIGURE 4 Comparison of dye-stained and wetting areas for I- and Λ-shaped cracks filled with rock fragment treatment (the wetting area was wetted by water, excluding the area wetted by Brilliant Blue FCF solution). The shaded part after the fitted line represented the 95% confidence interval.

FIGURE 5 Effect of crack inclusion (only CK, IR2, ΛR1.5, ΛS1.5, and IS2 treatments are shown here).

FIGURE 6 Effect of crack width (the crack width is the average of tests).

FIGURE 7 Effect of CK, IR1.5, VR1.5, and ΛR1.5 treatments crack configurations.

FIGURE 8 Effect of crack inclusion (a), crack width (b), and crack configuration (c) on the mean infiltration rate, dye-penetration depth, cumulative information, and wetting front depth. Different lowercase letters indicate significant differences between treatments at p <0.05 (e.g. a, b, and c indicate significant differences; a and ab indicate no significant differences). The error bars indicate the standard deviation of 3–4 replicates.

FIGURE 9 Dye coverage of soil vertical profiles and stained area ratio for the I- and Λ-shaped configurations filled with rock fragment are shown here.

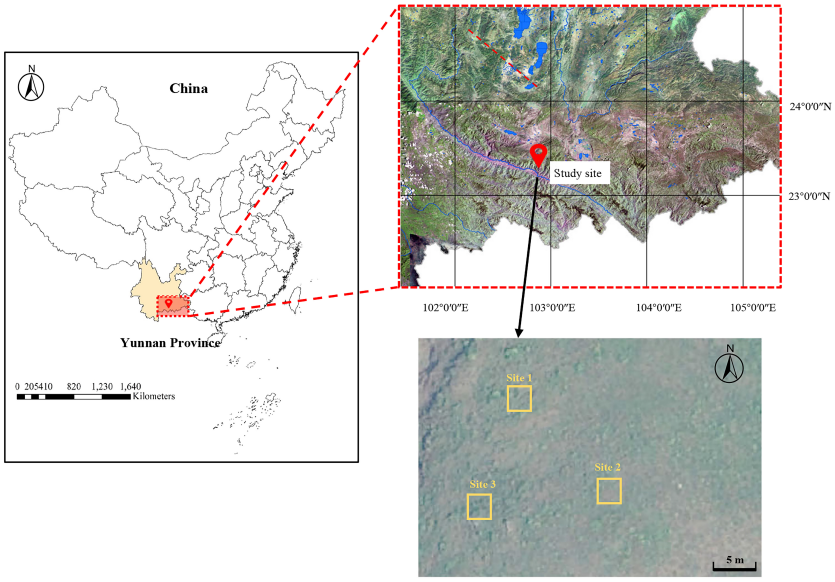

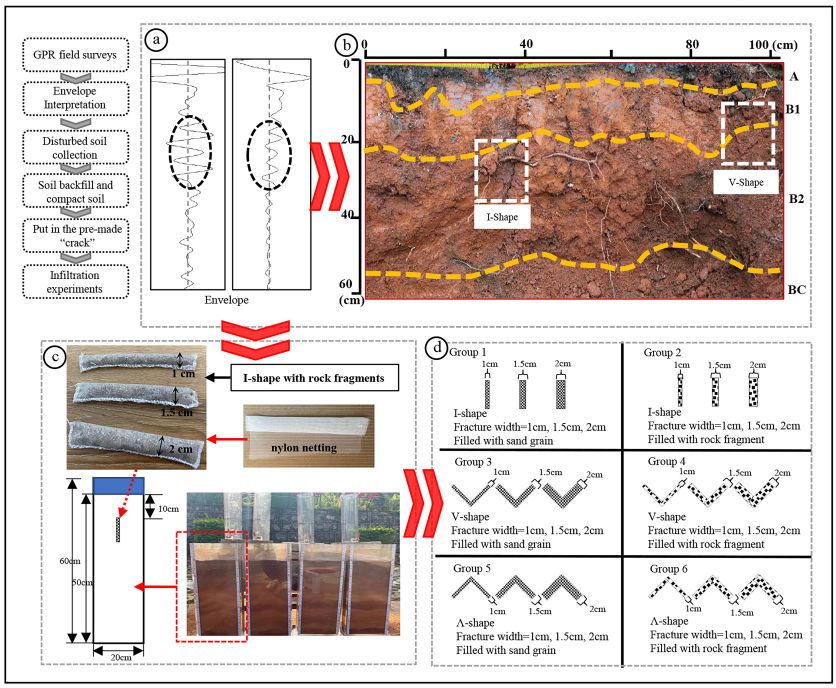

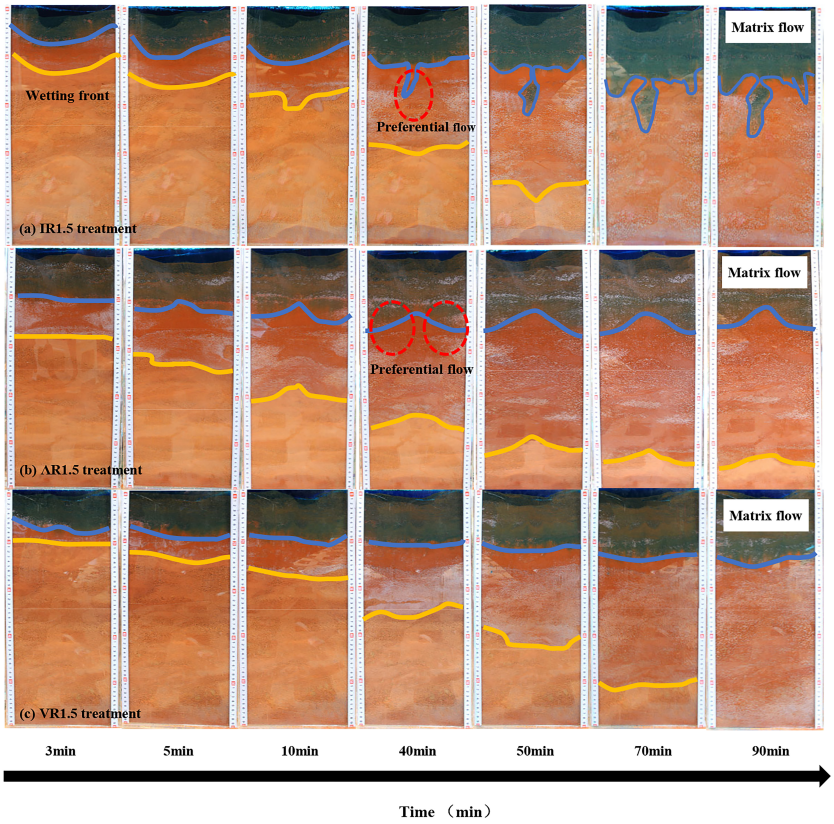

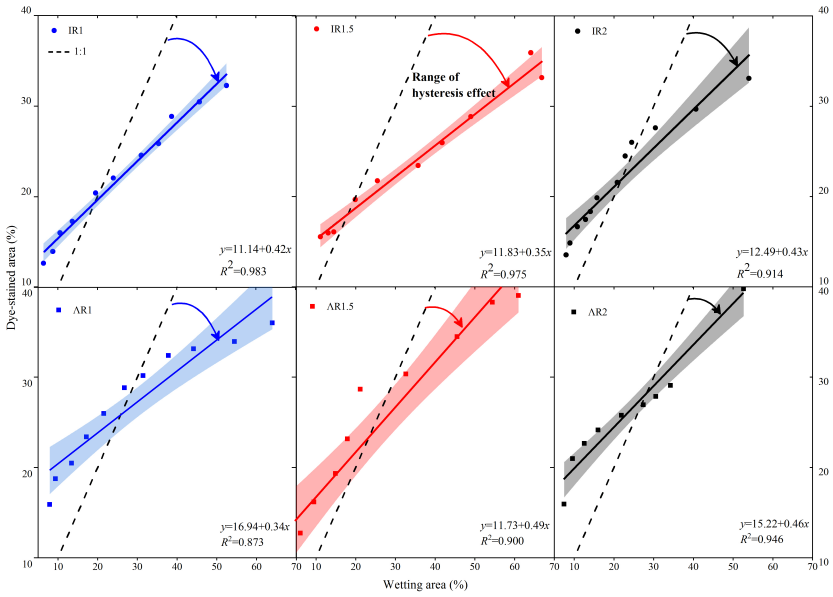

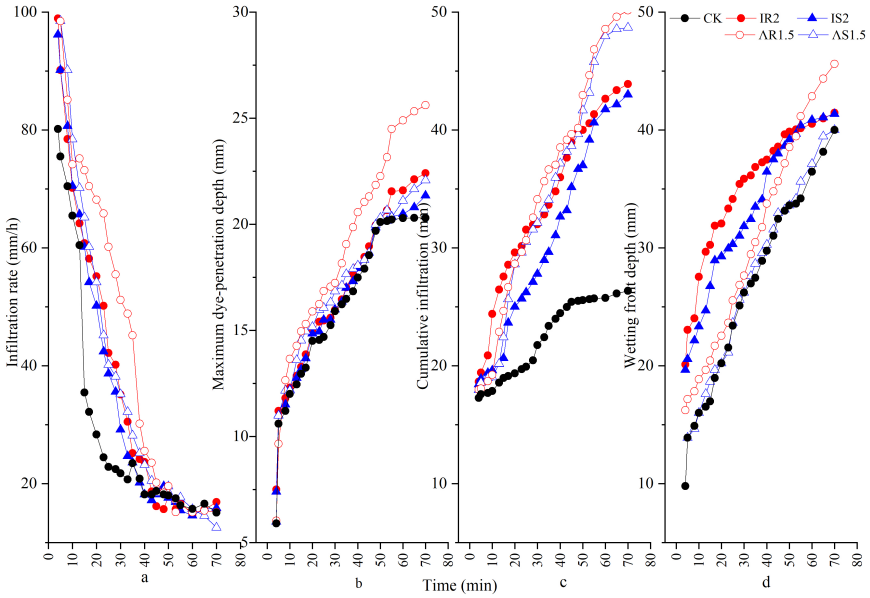

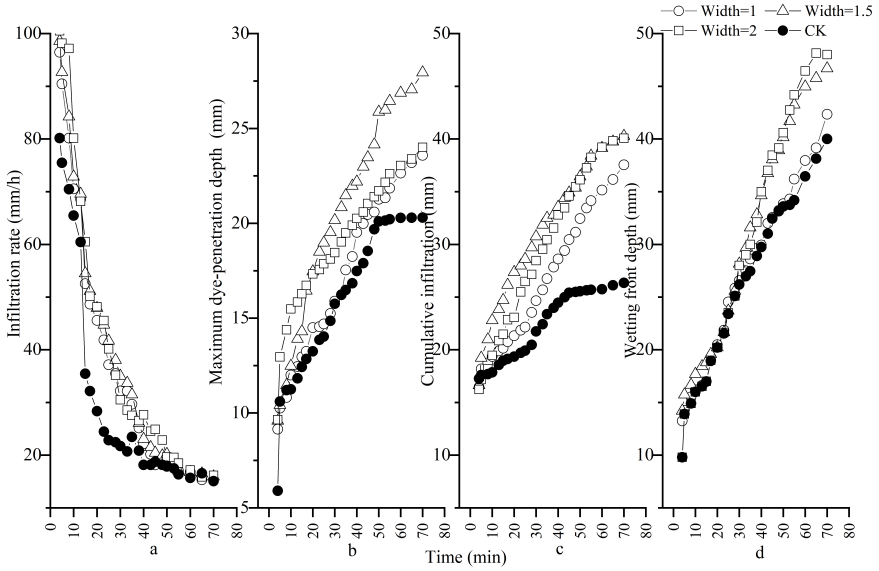

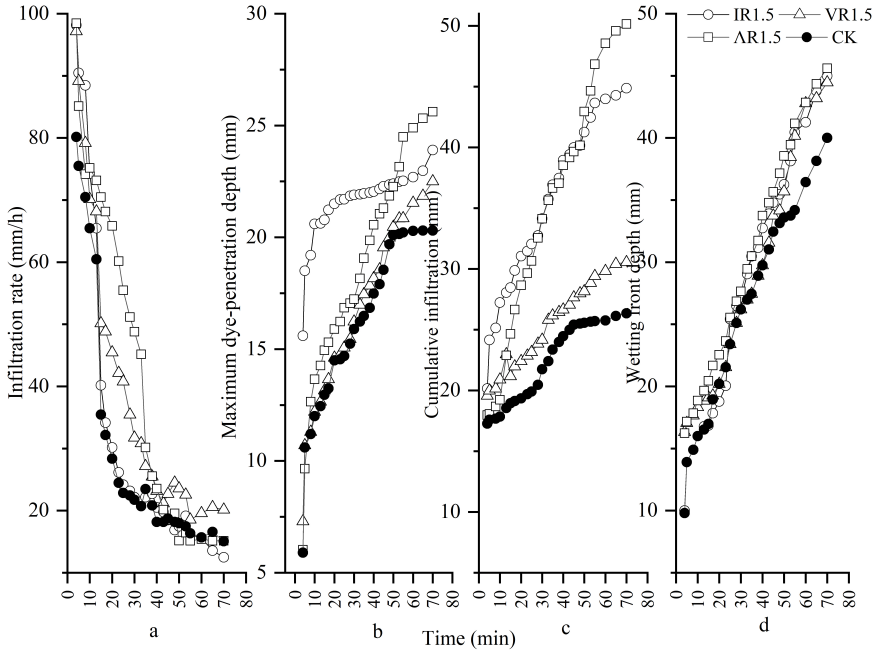

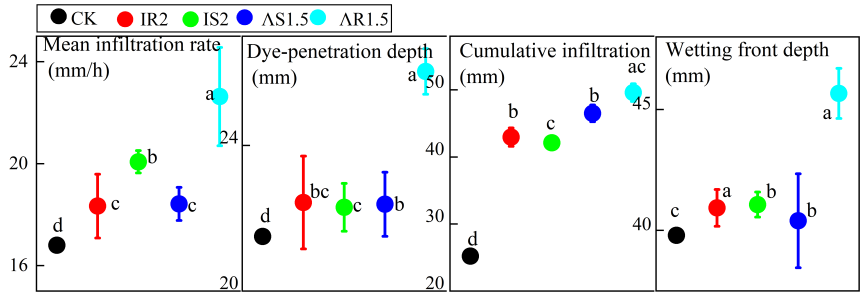

(a) Crack inclusion

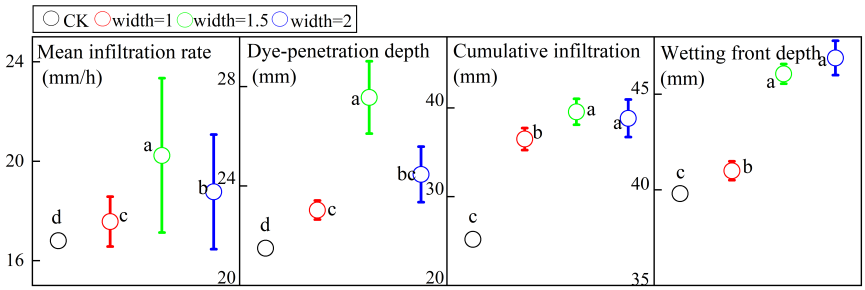

(b) Crack width

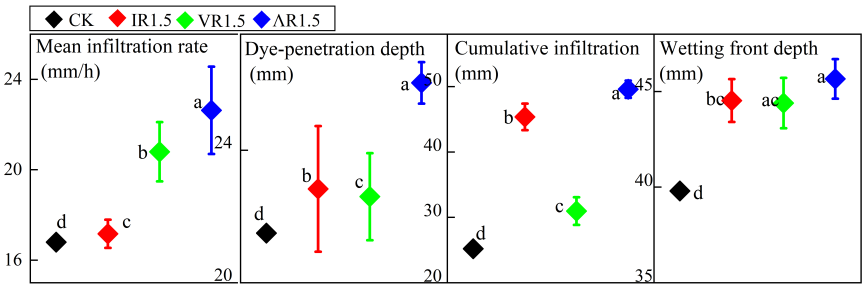

(c) Crack configuration

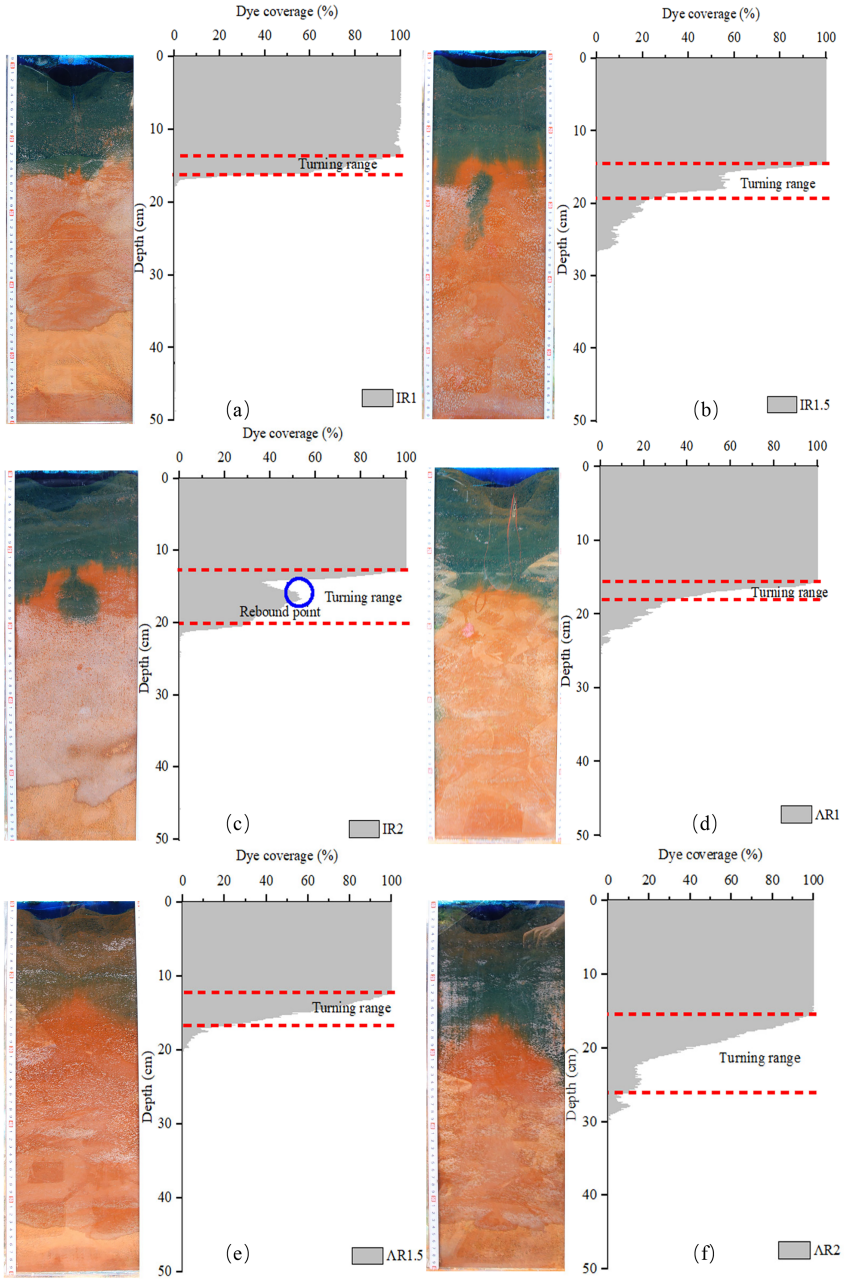

Figures caption:

FIGURE 1 Location of research area and the three study sites in Jianshui County, Yunnan Province, China.

FIGURE 2 Main steps of infiltration experiment: (a) identification of envelope curves on radargram; (b) soil profile at pedon 1 (yellow dotted lines represent the boundary between horizons, white dashed boxes represent cracks found during excavation); (c) Plexiglas columns for experiment and text device; and (d) experimental groups to be performed.

FIGURE 3 Infiltration process over time in different treatments (only IR1.5, ΛR1.5, and VR1.5 treatments are shown here), with blue lines indicating dye traces, yellow lines indicating moisture wetting front traces, and red dotted regions indicating that the preferential flow occurred after 40 minutes.

FIGURE 4 Comparison of dye-stained and wetting areas for I- and Λ-shaped cracks filled with rock fragment treatment (the wetting area was wetted by water, excluding the area wetted by Brilliant Blue FCF solution). The shaded part after the fitted line represented the 95% confidence interval.

FIGURE 5 Effect of crack inclusion (only CK, IR2, ΛR1.5, ΛS1.5, and IS2 treatments are shown here).

FIGURE 6 Effect of crack width (the crack width is the average of tests).

FIGURE 7 Effect of CK, IR1.5, VR1.5, and ΛR1.5 treatments crack configurations.

FIGURE 8 Effect of crack inclusion (a), crack width (b), and crack configuration (c) on the mean infiltration rate, dye-penetration depth, cumulative information, and wetting front depth. Different lowercase letters indicate significant differences between treatments at $p < 0.05$ (e.g. a, b, and c indicate significant differences; a and ab indicate no significant differences). The error bars indicate the standard deviation of 3–4 replicates.

FIGURE 9 Dye coverage of soil vertical profiles and stained area ratio for the I- and Λ-shaped configurations filled with rock fragment are shown here.

Hosted file

`Tables.docx` available at https://authorea.com/users/477882/articles/566289-investigating-the-effect-of-soil-cracks-on-preferential-flow-using-ground-penetration-radar-surveys-and-infiltration-experiment-in-karst-southwest-china